JOURNAL OF SPACECRAFT AND ROCKETS
Vol. 43, No. 6, November–December 2006

Simulations of Solid-Propellant Rockets: Effects of Aluminum Droplet Size Distribution

F. M. Najjar,* J. P. Ferry,† A. Haselbacher,‡ and S. Balachandar§
University of Illinois at Urbana–Champaign, Urbana, Illinois 61801

Flow modeling and simulation of solid-propellant rockets from first principles is quite challenging with several physical problems, including complex evolving geometries, turbulence, and multiphase flow with a chemically reactive disperse phase. To this end, a flexible simulation framework has been developed, in which multiphase flow computations are performed that include three-way coupling between phases (mixture–droplet–smoke), conservative coupling approach, and full heat release for the burning mechanisms. Results obtained from computations with burning aluminum droplets generating aluminum-oxide smoke are described for a generic rocket geometry. The effects of injected droplet size distribution obtained with two models are investigated and show the sensitivity of these distributions to the chamber flow dynamics, primarily at the nozzle inlet. The residence time and burning droplet diameter are verified by comparison with simple analytical predictions.

Nomenclature

C_p	=	specific heat at constant pressure, J/(kg · K)
C_s	=	concentration of smoke, kg/m^3
D_s	=	diffusion coefficient of smoke, m^2/s
d	=	diameter, m
e	=	total internal energy per unit volume, J/m^3
F	=	forces, N
h	=	heat of reaction, J/(kg · K)
k	=	conductivity, W/(m · K)
L	=	superdroplet loading factor
M	=	Mach number
M_R	=	molecular weight ratio
m	=	mass, kg
$\dot{m}$	=	mass flux rate, kg/m^2 s
N_{density}	=	number density
Pr	=	Prandtl number
p	=	pressure, Pa
q_i	=	ith component of heat-flux vector, W/m^2
Re	=	Reynolds number
S	=	source term
S_{ij}	=	ijth component of the strain rate tensor, 1/s
T	=	temperature, K
t	=	time, s
t_{res}	=	residence time, s
$\boldsymbol{u}$	=	velocity vector, $\boldsymbol{u} = \{u_1, u_2, u_3\}^T$, m/s
u_i	=	ith component of velocity vector, m/s
$\boldsymbol{v}_p$	=	droplet velocity vector, $\boldsymbol{v}_p = \{v_{p_1}, v_{p_2}, v_{p_3}\}^T$, m/s
$\boldsymbol{w}_s$	=	smoke velocity vector, $\boldsymbol{w}_s = \{w_{s_1}, w_{s_2}, w_{s_3}\}^T$, m/s
$\boldsymbol{x}$	=	coordinate vector, $\boldsymbol{x} = \{x, y, z\}^T$, m
x, y, z	=	Cartesian coordinates, m
γ	=	ratio of specific heats
η_c	=	collision efficiency
μ	=	dynamic viscosity coefficient, kg/(m · s)
ρ	=	density, kg/m^3
σ	=	variance
σ_{ij}	=	stress tensor, N/m^2
τ_p	=	droplet velocity time scale, 1/s
$\tau_{p,\theta}$	=	droplet temperature time scale, 1/s
τ_s	=	smoke velocity time scale, 1/s
$\tau_{s,\theta}$	=	smoke temperature time scale, 1/s
ϕ_p	=	droplet mass composition
χ	=	mass fraction
ψ	=	volume fraction

Operators

D/Dt	=	total derivative, $\partial_t + u_i \partial_i$
δ_{ij}	=	Kronecker delta
∂_i	=	partial spatial derivative
∂_t	=	partial time derivative

Subscripts and superscripts

bu	=	burning
dep	=	deposition
e	=	energy
i	=	ith component of vector
ij	=	ijth component of tensor
inj	=	injection
l	=	lth droplet
max	=	maximum
med	=	median
min	=	minimum
p	=	droplet
peak	=	peak
s	=	smoke
ρ	=	density
ρu	=	momentum

Received 22 April 2005; revision received 18 July 2005; accepted for publication 23 August 2005.

*Senior Research Scientist, Center for Simulation of Advanced Rockets; fnajjar@csar.uiuc.edu. Senior Member AIAA.
†Analyst, Metron, Inc., Center for Simulation of Advanced Rockets.
‡Principal Research Scientist, Center for Simulation of Advanced Rockets. Member AIAA.
§Professor, Department of Theoretical and Applied Mechanics. Senior Member AIAA.

I. Introduction

SIMULATING solid-propellant rocket motors (SRM) from first principles with minimal empirical modeling is a computationally challenging task. Modern multisegmented rocket motors are inherently three-dimensional and geometrically complex. As the propellant burns, the geometry changes in a time-dependent manner. The flow within the rocket is subsonic near the head end, but compressibility effects become important in the nozzle region. The flow transitions from a laminar state near the head end to a fully turbulent state farther downstream. The flow within the rocket is multiphase, because it contains droplets and smoke particles. The flow within the rocket chamber is chemically reacting, due to the burning

of metallic fuel droplets and in the nozzle region. The physical processes that account for these complexities are often interrelated and therefore require additional care in their computational modeling by including the appropriate source terms in the governing equations.

The focus of this paper is on the multiphase aspect of flow in SRMs. Modern propellants are laden with aluminum particles that compose up to 20% of total mass. As the propellant burns, the propellant–combustion interface regresses and the aluminum (Al) particles added to the propellant melt to form puddles. A complex mechanism follows, resulting in the release of Al droplets from the puddles and their injection into the accelerating core flow. A detailed summary of the history of Al particles originating within the propellant and entering into the motor chamber is discussed in Price and Sigman.[1] The initial size of Al droplets is found to vary from a few micrometers to a few hundred micrometers (typically 300–400 μm) (M. Alkema, Aerojet, Inc., private communication, 2005). Further, the droplets are released into strong crossflow and, hence, their initial Reynolds number (based on relative velocity and diameter) can be significant, as high as a few hundred. The primary reason for the inclusion of Al droplets into the solid propellant stems from the significant heat release obtained as the Al droplets burn to form aluminum oxides (Al_2O_3). Near-wall turbulence generated from the combustion process plays an important role in the dispersion of Al droplets. Burning of the Al droplets is thus spatially distributed inside the rocket chamber and influences the overall core flow, in contrast to the propellant combustion, which is confined to the surface. Inclusion of Al particles in the propellant, however, has other side effects. It leads to slag accumulation in submerged nozzles and the Al droplets and Al_2O_3 particles are the main source of nozzle scouring from particulate impaction.

The earliest descriptions of SRM core flow have focused on analytical methods[2–4] and one-dimensional models of the pressure rise in the rocket chamber.[5] More recent models are mainly based on two-dimensional analytical[6,7] and, especially, numerical, single- or two-phase flow using an Eulerian formalism for the droplets[8–13] or a Lagrangian formalism.[14–17] Many authors have chosen single-sized droplets and performed a series of simulations to determine the effects of droplet diameter.[16–19] Ciucci et al.[18] have performed three-dimensional simulations with Lagrangian droplets in the Ariane V motor using one-way coupling where the flow drives the droplet motion and no back coupling is allowed. They showed the complex Lagrangian droplet winding paths induced due to the flow dynamics.

An area that has not received a lot of attention is the size distribution of the droplets entering the chamber and how it affects the flow. Sabnis et al.[16] refer to Salita's quench-bomb investigations,[20] where the size distribution was found to be lognormal and bimodal. Typical values of the weighted mean diameter were 1.5 μm for the small particles, whereas the larger particles were 150 μm with a standard deviation of 0.2. However, Whitesides et al.[21] analyzed a reusable solid rocket motor (RSRM) production propellant, RSRM TH-H148, and concluded that a single lognormal or polynomial distribution did not adequately fit the measured droplet diameter distribution. Such contradictory conclusions indicate that the droplet size distribution is sensitive to the propellant formulation.

Despite the effort to model as much of the physics from first principles as possible, some of the key physical processes still need to be accounted for with empirical models. For example, the physical processes by which the Al droplets form at the propellant–combustion interface and get injected into the flow are still not fully understood.[1] Models for the droplet injection into the chamber have not been well quantified. Sabnis et al.[16] have proposed a simple model based on a predetermined number of "pulses" of new computational droplets at appropriate spatial locations during a certain time period. Similarly, a clear understanding is lacking of the process by which the larger droplets and particles fragment in the highly strained nozzle flow. As a result, empiricism is unavoidable in modeling these complex processes. Given such restrictions, the best computational approach is to study the sensitivity of the results to realistic variations in the empirical models and their parameters.

Here we focus on the uncertainty involved in the injection of Al droplets at the propellant combustion interface. The overall mass rate of Al injection is well defined from the local burn rate of the propellant and the mass fraction of Al in the propellant. What is not well understood is the size, velocity, and composition (Al vs Al_2O_3) spectra of the injected droplets. The popular approach is to use a lognormal distribution for the injected droplets. However, recent investigations of propellant packing have yielded more realistic distributions for the injected droplet distribution.[22] In the present work, we explore the sensitivity of the computed flow within the rocket core to variations in the injected droplet distributions. Three different injection distributions are considered and thereby the validity of the lognormal assumption is addressed.

The sensitivity analysis suggested here requires running many simulations with different empirical models and parameter values for the physical processes. Thus the computational framework must be designed in a flexible manner to allow activation and deactivation of different models as well as how they interact. In the present effort, all of the physical processes have been encapsulated in separate code modules and we have developed a framework for interfacing the various physics modules in a seamless manner.

The overall goal of the present effort is to perform detailed full-physics multiphase simulations of the flow inside the SRM, including both the burning droplets and the alumina smoke. The present computational capability fully recognizes the multidimensional, time-dependent, compressible, multiphase, reacting, turbulent nature of the problem. This comprehensive model will be described here. In particular, the present model incorporates three novel elements, which can be of use to other SRM simulation efforts.

First, we have developed an equilibrium Eulerian formulation[23] for the treatment of the fine smoke particles, which will be used in conjunction with a Lagrangian formulation for the larger Al droplets. The equilibrium Eulerian approach is computationally very efficient, has been verified to be quite accurate when used to represent small particles, and has been shown to capture important physics, such as preferential accumulation and turbophoretic migration of particles.[23]

Second, we have developed a stochastic injection framework that mimics the physical process by which Al droplets are introduced into the flow. This framework can be used to achieve any desired distribution for the injected droplets.

Third, in general it is difficult to accurately account for the heat release generated from the burning of the Al droplets. This difficulty arises from the fact that simple implementation of the droplet burn-rate models results in unphysically high mixture temperatures, well above the boiling point of Al_2O_3. A simple ad hoc fix has been to scale back the heat release to a fraction (usually 10–20%) of the actual value.[13] This approach will, however, underestimate the total heat release and therefore lead to incorrect prediction of the flow and thermal fields. The appropriate model of the physical process is to retain the aluminum oxide, which is the product of combustion, in the gaseous phase if the local mixture temperature is above the boiling point of the oxide. The oxide will convert to the condensed phase only when local temperature falls below the boiling point temperature. This complex regulation mechanism is an important advance that has been incorporated into the present droplet combustion model.

The paper is organized as follows: Section II describes the physical models. Section III outlines the computational framework within which the models are implemented. The problem setup is summarized in Sec. IV. Results are discussed in Sec. V. Section VI provides conclusions and a summary.

II. Physical Modeling

To perform accurate simulations of the complex flow inside the SRM chamber, sophisticated physical models for the evolution of gas mixture, aluminum droplets, and aluminum oxide smoke, as well as their interactions are required. One may think of such models as adding physical fidelity to a basic fluid-dynamic description.

The appropriate treatment of the aluminum droplets and smoke particles depends on their length and time scales. Table 1 presents the typical spatial and temporal scales of the flow as well as those of the Al droplets and smoke particles. The length and time scales

Table 1 Length and time scales of the three different phases

Phase	Length scale, μm	Time scale
Core flow	10	20.0 μs
Aluminum droplets	100	0.1 s
Smoke particles	1	10.0 μs

of the gaseous mixture are the Kolmogorov scales appropriate for a typical solid-rocket core flow, whereas those of the particulate fields are their response times as given by Ferry and Balachandar.[23] Based on the length- and time-scale ratios, the aluminum droplets are sufficiently large that a Lagrangian approach is adopted (see Sec. II.B). The fine oxide particles are considered sufficiently small that an Eulerian representation is appropriate. Here we use the equilibrium Eulerian approach to account for the smoke, which will be discussed in detail in Sec. II.F.

A. Gas Mixture

The time-dependent compressible Navier–Stokes equations govern the evolution of mass, momentum, and energy of the flow inside the rocket motor:

$$\begin{aligned}\partial_t \rho + \partial_j(\rho u_j) &= S_\rho \\ \partial_t(\rho u_i) + \partial_j(\rho u_i u_j) + \partial_i p - \partial_j \sigma_{ij} &= S_{\rho u,i} \\ \partial_t e + \partial_j((e+p)u_j) - \partial_j(\sigma_{ij}u_i - q_j) &= S_e \end{aligned} \tag{1}$$

The summation convention is used throughout this paper. The symbols ∂_t and ∂_j denote the partial differential operators $\partial/\partial t$ and $\partial/\partial x_j$, and e the total energy density, given for an ideal gas by

$$e = e(p, \boldsymbol{u}) = p/(\gamma - 1) + \tfrac{1}{2}\rho u_i u_i \tag{2}$$

The stress tensor σ_{ij} is a function of the dynamic viscosity μ and velocity vector $\boldsymbol{u}$:

$$\sigma_{ij} = \sigma_{ij}(\mu, \boldsymbol{u}) = \mu(T) S_{ij}(\boldsymbol{u}) \tag{3}$$

where the strain rate tensor S_{ij} is defined as

$$S_{ij} = S_{ij}(\boldsymbol{u}) = \partial_j u_i + \partial_i u_j - \tfrac{2}{3}\delta_{ij}\,\partial_k u_k \tag{4}$$

The dynamic viscosity μ is either assumed to be constant or related to the temperature T by Sutherland's law. Finally, q_i is the ith component of the heat-flux vector, defined as

$$q_i = q_i(k, T) = -k\partial_i T = -(\mu C_p/Pr)\partial_i T \tag{5}$$

The temperature is related to the density and the pressure by the ideal gas law

$$p = \rho R T \tag{6}$$

where R is the gas constant. Throughout we use $Pr = 0.72$ for laminar flows.

Physical components interact with the mixture through the source terms on the right-hand side of Eq. (1); that is,

$$S_\rho = S_\rho^s + S_\rho^p, \qquad \boldsymbol{S}_{\rho u} = \boldsymbol{S}_{\rho u}^p + \boldsymbol{S}_{\rho u}^s, \qquad S_e = S_e^p + S_e^s \tag{7}$$

It is important to note that these source terms may represent fluxes or genuine volume sources. These source terms will be described in the sections to follow.

B. Aluminum Droplets

The Lagrangian evolution equations for the droplet position vector $\boldsymbol{x}_p$, velocity vector $\boldsymbol{v}_p$, and temperature T_p are

$$\begin{aligned}\frac{\mathrm{d}\boldsymbol{x}_p}{\mathrm{d}t} &= \boldsymbol{v}_p, \qquad \frac{\mathrm{d}\boldsymbol{v}_p}{\mathrm{d}t} = \frac{1}{\tau_p}[\boldsymbol{u}(\boldsymbol{x}_p) - \boldsymbol{v}_p] \\ \frac{\mathrm{d}T_p}{\mathrm{d}t} &= \frac{1}{\tau_{p,\theta}}[T(\boldsymbol{x}_p) - T_p] \end{aligned} \tag{8}$$

with the time scales τ_p and $\tau_{p,\theta}$ given by

$$\tau_p = \frac{\rho_p d_p^2}{18\mu f(Re_p)}, \qquad \tau_{p,\theta} = \frac{C_{p,p}\rho_p d_p^2}{12 k f_\theta(Re_p)} \tag{9}$$

where ρ_p, d_p, and $C_{p,p}$ are the droplet density, diameter, and specific heat, respectively. A simple drag law is invoked to evolve the droplets. Because the Reynolds number of the droplets is expected to be larger than unity, a standard correction to the Stokes drag is used:

$$f(Re_p) = 1 + 0.15\,Re_p^{0.687}, \qquad f_\theta(Re_p) = 1 + 0.3\,Re_p^{\frac{1}{2}} Pr^{\frac{1}{3}} \tag{10}$$

where the droplet Reynolds number is given by

$$Re_p = \rho \|\boldsymbol{u}(\boldsymbol{x}_p) - v_p\| d_p/\mu \tag{11}$$

Here $\boldsymbol{u}(\boldsymbol{x}_p)$ corresponds to the mixture velocity at the droplet location. In the context of the rocket problem, these drag and heat-transfer laws for the droplets have at least two shortcomings. First, the drag force may be significantly influenced by the evaporation and combustion processes. Second, the strong acceleration of the flow in the nozzle region will require more accurate correlations and will also result in the break-up of the larger droplets. Hence, these equations of motion serve only as a first approximation. Efforts are currently underway to improve these correlations.[24]

Our computational framework allows for the fact that the droplets are generally multicomponent in nature. For example, in the present context each droplet is a mixture of molten Al and Al_2O_3 in the form of an oxide cap. Even as the droplet is injected at the propellant combustion interface, part of it is in the form of aluminum oxide.[25] As the droplet moves through the core flow, Al evaporates and burns. There are several mechanisms for droplet coalescence, collision, and agglomeration: the droplet agglomeration at the propellant surface, taken care of by the models described in Sec. II.G, the droplet–smoke collision discussed in Sec. II.D, the droplet–droplet coalescence in the nozzle, and smoke–smoke agglomeration. Of these mechanisms, only droplet–smoke collision will be modeled in the current study. Briefly described, the amount of Al_2O_3 in the droplet increases as the droplet collects the surrounding oxide smoke particles through a scavenging process. Thus the droplet starts out being mostly Al, but ends up being mostly alumina oxide.

Here we track the composition of each droplet by evolving the mass of each of the constituents individually as follows:

$$\frac{\mathrm{d}m_{\mathrm{Al}}}{\mathrm{d}t} = -\dot{m}_{\mathrm{bu}} \tag{12}$$

$$\frac{\mathrm{d}m_{\mathrm{Al_2O_3}}}{\mathrm{d}t} = \dot{m}_{\mathrm{dep}} \tag{13}$$

where the right-hand sides represent the depletion of aluminum due to the evaporation and burning and the collection of oxide particles by collision and agglomeration, respectively. From the mass and material properties of each of the components we can calculate the effective density and diameter of the droplet as

$$\rho_p = \left(m_{\mathrm{Al}} + m_{\mathrm{Al_2O_3}}\right)\left(\frac{m_{\mathrm{Al}}}{\rho_{\mathrm{Al}}} + \frac{m_{\mathrm{Al_2O_3}}}{\rho_{\mathrm{Al_2O_3}}}\right)^{-1} \tag{14}$$

$$d_p = \sqrt[3]{\frac{6}{\pi}\left(\frac{m_{\mathrm{Al}}}{\rho_{\mathrm{Al}}} + \frac{m_{\mathrm{Al_2O_3}}}{\rho_{\mathrm{Al_2O_3}}}\right)} \tag{15}$$

C. Burn Rate Model with Full Heat Release

The combustion of Al droplet consists of a complex process. Once the ambient temperature exceeds the oxide melting point, the oxide shell around the droplet cracks and exposes the liquid Al. Aluminum vaporizes, advects, and diffuses away from the droplet and reacts with the oxidizers (such as O_2, H_2O, CO_2) that are present. A reaction front forms around the droplet and the primary product of

combustion is aluminum oxide. Although the reaction thus takes place in the gas phase, here we recognize that on the scale of the rocket, we will not be able to resolve the gas phase chemistry that occurs around each droplet. Thus we treat the burning of each droplet in a Lagrangian manner. The burn rate of a droplet is assumed to follow a general power-law relation dependent on the droplet diameter, local pressure and temperature, and oxidizer concentration. Here we use the correlation proposed by Widener and Beckstead[25] as the model for the Al droplet burn rate:

$$\dot{m}_{\mathrm{bu}} = c\rho_{\mathrm{Al}} T^{1.57}(\boldsymbol{x}_p)\, p^{0.2}(\boldsymbol{x}_p)\, \chi_{\mathrm{eff}}^{0.39} \mathcal{D}_{\mathrm{rel}} d_p^{1.1} \psi_{\mathrm{Al}} \tag{16}$$

where the constant of proportionality c has the value (in SI units) 2.885×10^{-13}, whereas the effective oxidizer mass fraction, χ_{eff}, is defined in terms of the individual components as

$$\chi_{\mathrm{eff}} = \chi_{\mathrm{O_2}} + 0.58\chi_{\mathrm{H_2O}} + 0.22\chi_{\mathrm{CO_2}} \tag{17}$$

In situations where the different oxide components are not individually followed, χ_{eff} can be computed based on conditions representative of the core flow within the rocket chamber. In Eq. (16), $\mathcal{D}_{\mathrm{rel}}$ is given by

$$\mathcal{D}_{\mathrm{rel}} = 1 + 2.7\chi_{\mathrm{H_2}} \tag{18}$$

The burn-rate model does not take into account that part of the droplet is in the form of an oxide cap. Here we account for the presence of the oxide cap by scaling the burn rate with the volume fraction of aluminum as

$$\psi_{\mathrm{Al}} = \frac{\phi_{\mathrm{Al}}\rho_{\mathrm{Al_2O_3}}}{\phi_{\mathrm{Al}}\rho_{\mathrm{Al_2O_3}} + (1-\phi_{\mathrm{Al}})\rho_{\mathrm{Al}}} \tag{19}$$

where the mass fraction of aluminum ϕ_{Al} within the droplet is defined as

$$\phi_{\mathrm{Al}} = m_{\mathrm{Al}} \Big/ \left(m_{\mathrm{Al}} + m_{\mathrm{Al_2O_3}}\right) \tag{20}$$

This burn-rate model assumes the combustion of an individual droplet in a quiescent ambient medium. Conditions under which the Al droplets burn within the rocket differ from this ideal picture in several significant ways. For example, there is strong crossflow between the droplet and the surrounding gas flow in a rocket. Furthermore, interference between the burning of neighboring droplets may not always be negligible. For lack of better models, we ignore such complexities and use the preceding burn rate model,[25] as it has been mainly used in the literature.[13,19]

The burn rate model, when used naively, often leads to locally unphysical values of the gas mixture temperature, resulting in values far in excess of the boiling point of Al_2O_3 (typically around 4000 K). An adhoc fix for this problem has been to restrict the heat release from combustion to be only a fraction of the actual value.[13] This is not a satisfactory solution, because it leads to an unphysical lower total heat release to the gas phase. The proper solution to this problem lies in the recognition of how the heat is released in the combustion process. The total heat release h of the combustion process is composed of contributions arising from several subprocesses:

$$h = -h_{\mathrm{ev}} + h_{\mathrm{reac}} + h_{\mathrm{cond}} + h_{\mathrm{solid}} \tag{21}$$

The terms in Eq. (21) correspond to the heat of evaporation from $\mathrm{Al}(l)$ to $\mathrm{Al}(g)$, the heat of reaction from $\mathrm{Al}(g)$ to $\mathrm{Al_2O_3}(g)$, the heat of condensation from $\mathrm{Al_2O_3}(g)$ to $\mathrm{Al_2O_3}(l)$, and the heat of solidification from $\mathrm{Al_2O_3}(l)$ to $\mathrm{Al_2O_3}(s)$. Typical values for these quantities are shown in Table 2.[13,19]

The table clearly shows that the bulk of heat release occurs in the condensation process of $\mathrm{Al_2O_3}(g) \rightarrow \mathrm{Al_2O_3}(l)$. Localized hotspots appear in the gas phase when the heat of combustion is applied as a whole, without recognizing the different contributions. From physical reasoning it can be argued that provided the local temperature exceeds the boiling point of the oxide, the combustion reaction should proceed only as far as $\mathrm{Al}(g) \rightarrow \mathrm{Al_2O_3}(g)$ and the condensation process cannot locally occur. In such regions, the burning of Al droplets must result in the release of only the heat of reaction and the oxide must remain in the gas phase. This points to the need to monitor Al_2O_3 in the gas phase, in addition to the smoke particulate phase and the combustion process, which can be denoted symbolically as

Table 2 Typical values for heats of reaction in Eq. (21)

Quantity	Value, J/(kg · K)
h_{ev}	8,240.0
h_{reac}	7,157.0
h_{cond}	29,326.0
h_{solid}	0.0

$$2\mathrm{Al}(l) + 3\mathrm{O}(g) \rightarrow \alpha\mathrm{Al_2O_3}(s) + (1-\alpha)\mathrm{Al_2O_3}(g) \tag{22}$$

where α is the fraction that condenses to solid state as smoke particles. When the local temperature is greater than the oxide boiling point $T_{b,\mathrm{Al_2O_3}}$, then $\alpha = 0$. When T is just less than $T_{b,\mathrm{Al_2O_3}}$, then α will be determined such that local gas temperature will not exceed $T_{b,\mathrm{Al_2O_3}}$. When $T \ll T_{b,\mathrm{Al_2O_3}}$, then $\alpha = 1$, and furthermore if there is any oxide that still remains in the gas phase it will condense to form oxide smoke and increase the associated heat of condensation. In the absence of this regulation mechanism, wildly varying thermal fields are often generated with very high local temperatures, which in turn can cause numerical instabilities. By incorporating the physically motivated regulation process, we obtain a very robust Al combustion model.

D. Oxide Cap Growth

The oxide caps of the aluminum droplets grow as the droplets collide and agglomerate with the oxide–smoke particles. This collision process is driven by the relative velocity between the droplet and the surrounding smoke particles. Thus the volume swept by the droplet in unit time is given by $(\pi/4)d_p^2\|\boldsymbol{v}_p - \boldsymbol{u}(\boldsymbol{x}_p)\|$, where we neglect the diameter of the smoke particle in comparison to the droplet diameter. The deposition rate $\dot{m}_{\mathrm{dep}}$ is then given by the number of smoke particles within the relative volume swept and is therefore proportional to the local concentration C_s of oxide smoke:

$$\dot{m}_{\mathrm{dep}} = (\pi/4)d_p^2\|\boldsymbol{v}_p - \boldsymbol{u}(\boldsymbol{x}_p)\|C_s\eta_c \tag{23}$$

Because of the effect of local hydrodynamics not all smoke particles inside the swept volume will end up colliding and agglomerating with the droplet. Furthermore, the above analysis ignores the evaporation of Al from the droplet and the complex combustion process around each droplet. These local complex phenomena are usually accounted for through the efficiency of collision and agglomeration η_c (Ref. 26). Here for lack of thorough understanding of the complex process in the literature, we simply take $\eta_c = 0.25$.

E. Lagrangian–Eulerian Coupling

As a result of the burning process, the aluminum droplets influence the mass, momentum, and energy of both the gas mixture and the oxide smoke field. This leads to coupling of the Lagrangian droplet back onto the carrier gas mixture. In the following, the subscript l denotes the source terms arising from the lth droplet. The source terms arising from all droplets within a finite volume cell are assumed to contribute to that cell only. Provided that the number of droplets per cell is significant, the resulting Eulerian field that influences the mixture and smoke evolution will be sufficiently smooth, and hence close to the true influence of the Lagrangian droplet field on the gas mixture. As the number of droplets per cell decreases (e.g., due to computational limitations), some spatial smoothing must be employed before the source terms are used to evolve the mixture and smoke fields.

As the droplets burn, oxidizers are consumed, and based on the stoichiometric relation given in Eq. (22), we have the following mass source for the gas mixture:

$$S_{\rho,l}^{p} = L\dot{m}_{\mathrm{bu},l}(1 - M_R) \tag{24}$$

where L represents the ratio of real droplets to the computational ones and $M_R = M_{Al_2O_3}/(2M_{Al})$ corresponds to the molecular weight ratio. The motivation for and the definition of the parameter L are given in Sec. III. The momentum source of the droplet on the mixture is

$$\boldsymbol{S}^p_{\rho u,l} = L\boldsymbol{F}_{p,l} + L\dot{m}_{\mathrm{bu},l}\boldsymbol{v}_{p,l} + S^p_{\rho,l}\boldsymbol{u}(\boldsymbol{x}_{p,l}) \tag{25}$$

where the drag force on the lth droplet is given by

$$\boldsymbol{F}_{p,l} = -(\pi/6)d^3_{p,l}(\rho_{p,l}/\tau_{p,l})(\boldsymbol{v}_{p,l} - \boldsymbol{u}(\boldsymbol{x}_{p,l})) \tag{26}$$

Finally, the energy source term is

$$S^p_{e,l} = \boldsymbol{S}^p_{\rho u,l}\cdot\boldsymbol{u}(\boldsymbol{x}_{p,l}) + L\dot{m}_{\mathrm{bu},l}h_b + L\dot{m}_{\mathrm{cond},l}h_c \tag{27}$$

where the effective heat release h_b of the combustion process recognizes the fact that it may or may not involve heat of condensation:

$$h_b = \alpha h + (1-\alpha)(-h_{ev} + h_{\mathrm{reac}}) \tag{28}$$

The last term of Eq. (27) arises from the fact that as the local temperature dips below the boiling point of the oxide, some of the Al_2O_3 gas will condense to the solid phase and give out the heat of condensation. Here $\dot{m}_{\mathrm{cond},l}$ is the mass rate at which oxide condenses and $h_c = h_{\mathrm{cond}} + h_{\mathrm{solid}}$ is the associated heat of release.

The Lagrangian treatment of the droplets must also couple to the equilibrium Eulerian treatment of the oxide smoke (see Sec. II.F) Each droplet acts as a local source of oxide–smoke particles. Further, each droplet serves as a local sink of oxide smoke through the collision and agglomeration process. The net source term for the evolution of the smoke concentration from the lth droplet is given by

$$S^p_{s,l} = L[(\dot{m}_{\mathrm{bu},l} + \dot{m}_{\mathrm{cond},l})M_R - \dot{m}_{\mathrm{dep},i}] \tag{29}$$

This equation accounts for the possibility that some of the oxide that remains in the gas phase can be contributing to the smoke particle concentration through the condensation process.

F. Oxide Smoke Particles

In the limit of very fine particles, one can use the modified density approach to evolve the smoke concentration field. In this case, one assumes that the smoke advects with the surrounding gas velocity; thus, only the smoke concentration field needs to be evolved as a scalar field. This approach has the great advantage that one avoids solving additional momentum equations for the smoke phase. However, this approach ignores the fact that the smoke particles do not travel perfectly with the gas and, as a result, exhibit inertial effects such as preferential accumulation and wall impaction.

An Eulerian approach to the smoke field avoids this drawback by computing the smoke phase velocity separately from the gas velocity. However, this approach suffers from the need to solve an additional set of momentum equations for the smoke phase. This difficulty becomes unmanageable if one desires to track many different sizes of smoke particles, because each size bin will involve a set of momentum equations.

Ferry and Balachandar[27] have developed an equilibrium Eulerian method for simulating the small, but finite-sized, smoke particles, which combines the advantages of the modified density and Eulerian methods. The present approach is nearly as fast as the modified density method, since it does not require solving the momentum equations for the smoke velocity. In this process, they also eliminate the numerical issue of stiffness associated with solving the momentum equations for very small particles.[27] Yet this approach accurately accounts for important inertial physics such as preferential accumulation and wall impaction that depend on the subtle departure of the smoke particle velocity from the surrounding gas velocity. The accuracy and efficiency of this approach have been thoroughly tested and documented for canonical turbulent flows.[27]

In the equilibrium Eulerian approach, the velocity field of the smoke $\boldsymbol{w}_s$ is expressed as an explicit expansion in terms of the local gas mixture velocity $\boldsymbol{u}$ as

$$\boldsymbol{w}_s = \boldsymbol{u} - \tau_s(D\boldsymbol{u}/Dt) \tag{30}$$

and the time scale of the smoke particles is

$$\tau_s = \rho_s d_s^2 \big/ 18\mu \tag{31}$$

where d_s is the diameter of the smoke particles and D/Dt is the total derivative following the fluid element. Equation (30) can be interpreted as follows: In regions with flow acceleration or deceleration (nonzero $D\boldsymbol{u}/Dt$), the particle response will be different from that of the fluid, resulting in a relative velocity $(\boldsymbol{w}_s - \boldsymbol{u})$ that will be proportional to particle Stokes number (defined as the ratio of the particle time scale to the local fluid one). Equation (30) presents only the leading-order term in the expansion. If necessary, additional terms in the expansion can be included, and furthermore, other sources of particle relative motion such as inertial lift force can be incorporated into this formalism.[28]

The smoke field acts as a momentum source for the mixture through

$$\boldsymbol{S}^s_{\rho u} = -LM_R\dot{m}_{\mathrm{bu},l}\boldsymbol{w}(\boldsymbol{x}_{p,l}) \tag{32}$$

The equilibrium formulation can be extended to the temperature field as well.[28] A straightforward analysis yields the following expansion for the smoke temperature:

$$T_s = T - \tau_{s,\theta}(DT/Dt) \tag{33}$$

where T_s is the smoke temperature, T corresponds to the gas temperature, and $\tau_{s,\theta}$ is the thermal response time of the particle. $\tau_{s,\theta}$ is expressed in terms of the specific heat $C_{p,s}$ of the smoke particles and the thermal conductivity k of the gas as

$$\tau_{s,\theta} = C_{p,s}\left(\rho_s d_s^2 \big/ 12k\right) \tag{34}$$

The physical interpretation of Eq. (33) is similar to that of Eq. (30). The local material derivative of temperature acts as the source and contributes to the differential temperature between the smoke particles and the surrounding gas mixture.

Equations (30) and (33) demonstrate that the velocity and temperature fields of the smoke particles can be readily obtained from those of the gas mixture. A significant advantage of this approach is that the velocity and thermal fields of different-sized particles differ only through their momentum and thermal time scales. Thus, the velocity fields of polydisperse smoke systems, classified in terms of different size bins, can easily be computed.

The only differential equation to be solved for the smoke phase is the advection–diffusion equation for the concentration field. The smoke particles are represented by a continuum concentration field, denoted by $C_s(\boldsymbol{x}, t)$, whose evolution is given by

$$\frac{\partial C_s}{\partial t} + \nabla\cdot(\boldsymbol{w}_s C_s) = \nabla\cdot(D_s\nabla C_s) + S^p_s \tag{35}$$

where the equilibrium Eulerian velocity is used to advect the smoke particles, and D_s is the diffusion coefficient, which accounts for the collisional and shear-induced diffusion of particles. In general, the evaluation of the diffusion coefficient can be complex, exhibiting complicated nonlinear dependence on the local smoke concentration itself.[29] Here, for simplicity, the diffusivity is considered to be a constant. The source term in Eq. (35) is given by a sum in computational cells over all of the droplets, whose individual contributions are given in Eq. (29).

G. Stochastic Droplet Injection Algorithm

An important component in the Lagrangian representation of aluminum droplets in SRM simulations is an appropriate description of the injection process at the propellant surface. In the past, several efforts in the literature have simplified the injection process to be at a fixed rate both temporally and spatially or with temporal pulsations.[16–19] However, the actual ejection mechanism, as observed in experiments, is random in space and time.

An accurate representation of the injection process is central to the predictive capability of the numerical simulation. The size, momentum, energy, and composition of the droplets at the time of their

injection critically determine their subsequent evolution. Through back-coupling the Al droplets in turn influence the gas mixture and smoke evolution. Thus, it can be argued that the overall prediction depends strongly on the droplet injection process. Despite this importance, as stated in the Introduction, the details of the complex process of droplet injection are not well understood.

Visualizations of aluminized propellant in experiments show that as burning proceeds, the micrometer-sized aluminum particles included in the propellant melt, agglomerate, and form larger molten puddles on the propellant surface (M. Beckstead, private communication, 2004). Periodically, either the entire puddle or parts of it are torn off the propellant surface by the hot gas to form droplets of mostly aluminum. Based on such described physical process, associated with each surface panel of the propellant (referred to numerically as *tile*, corresponding to a face of the surface grid), a molten puddle is maintained numerically, which, in general, comprises several material constituents.

Thus, it is important to construct a mathematical and computational framework that will allow us to experiment easily with different probability distributions for the injected droplet size and other related quantities. The injection process needs to provide the following information at each time step: the number of droplets injected into the chamber, their coordinates of the position on the injected surface, and their initial mass, momentum components, and energy. A Markovian-based approach for the droplet injection that mimics the physical mechanism occurring on the propellant surface has been developed. Hence, given a PDF for the injected droplet-size, the algorithm insures that droplets are injected randomly in space and time with the imposed PDF. Five distinct steps are required for droplet generation: droplet PDF selection, puddle initialization, puddle augmentation, puddle depletion, and droplet injection.

In the present study, we have selected two droplet-size PDF models: one is based on specific distribution for a propellant from previous work,[16] and the second is obtained from new agglomeration models from propellant packing code.[22] These models are

1) *Logarithmic normal distribution (LND):* Given a median droplet diameter d_{med} and a standard deviation σ of $\ell_n(d_{\text{med}})$, the lognormal distribution to determine the diameter of the next droplet to be injected is

$$Pr(d) = \left(1\Big/\sqrt{2\pi}\sigma d\right)\exp\left\{-(1/2\sigma^2)[\ell_n(d/d_{\text{med}})]^2\right\} \tag{36}$$

2) *Skewed logarithmic distribution (SLD):* Given peak, minimum, and maximum droplet diameter d_{peak}, d_{min}, d_{max}, respectively, and a standard deviation σ of $\ell_n(d_{\text{med}})$, the skewed distribution is formulated as

$$Pr(d) = \left[1-(d/d_{\max})^2\right]\left[1-(d_{\min}/d)^2\right] \times \exp\{-(1/2\sigma^2)[\ell_n(d)-\alpha]^2\} \tag{37}$$

where α is computed as

$$\alpha = \ell_n(d_{\text{peak}}) + \frac{2\sigma^2}{\left[(d_{\max}/d_{\text{peak}})^2 - 1\right]} \tag{38}$$

Further details on how the skewed logarithmic distribution is obtained are given by Jackson et al.[22]

III. Numerical Implementation and Computational Framework

The physical models described in Sec. II have been implemented in the code suite RocfluidMP.[28,30] For unsteady flows, the governing equations are integrated in time using a fourth-order accurate Runge–Kutta scheme. The remainder of this section describes the numerical implementation of the various physical modules in more detail.

The basic geometric features of solid-propellant rockets can be represented easily by block-structured grids. The block-structured code is based on a cell-centered finite-volume approach. The inviscid fluxes are computed from a central scheme augmented with an adaptive blend of second and fourth differences; see Jameson et al.[31] The viscous fluxes are computed from face-centered gradients. The code is parallelized using MPI,[32] based on the underlying block decomposition. The block-structured code and its parallel performance on large-scale systems are described in more detail by Blazek.[33]

The Lagrangian droplet evolution physical module is also parallelized using MPI. However, the numerical implementation is slightly different from that for the mixture because variable message lengths have to be used at every Runge–Kutta stage. Unlike the mixture where the Eulerian-based grid variables are consistently communicated, the Lagrangian droplets move through the various domains into which the rocket chamber has been decomposed. Their dynamic evolution in the computational domain requires a similar parallel communication pattern.

The numerical implementation of the smoke evolution is similar to that of the mixture. The only difficulty specific to smoke evolution is that the use of a central scheme for the convective fluxes can produce negative values of concentration because there is no counterbalancing pressure term. To overcome this numerical difficulty, clipping has been invoked. In the near future, positivity-preserving schemes are being implemented. The parallel implementation of the smoke particles follows directly that of the mixture field.

A. Computational Droplets

For aluminum droplet evolution, an important constraint in the Lagrangian representation pertains to the actual number of droplets that can be be tracked. For example, in the space shuttle redesigned solid-propellant rocket boosters, the core flow is over a length of 33 m with an initial inner radius of 0.78 m. An aluminum droplet of 20% by mass loading in the propellant will result in approximately 10^{15} droplets with a mean diameter of 100 μm within the rocket chamber. For smaller lab-scale motors, this number is significantly lower, but still on the order of several billion. Hence, it is virtually impossible to represent each and every real droplet in the computation. We further note that owing to the random injection of the droplets and their subsequent chaotic evolution inside the rocket due to core-flow turbulence, the instantaneous distribution of droplets and its influence on the core flow is stochastic. In the computations with fewer computational droplets the true stochastic influence of all the droplets must be adequately approximated.

To address these issues in the present computational framework, we consider each computational droplet to be a "superdroplet" (or a cluster of droplets) that accounts for L real droplets, where L is given by the ratio of the number of total real droplets to computational droplets; that is, $L = N_{\text{real}}/N_{\text{comp}}$. Two simple but somewhat conflicting criteria dictate the choice of this parameter L. On the one hand, the number of computational droplets must be chosen so that the computational cost of Lagrangian tracking will be in approximate balance with the computational cost of advancing the flow and the smoke fields. In the present implementation this cost balance is achieved for about six particles per cell. On the other hand, the number of computational droplets within each cell should be sufficiently large that a simple sum over all the particles within each cell should provide an adequately accurate representation of the actual effect of all the droplets. Otherwise, as the number of computational droplets within a finite-volume cell decreases, the randomness in the computed mass, momentum, and energy feedback of these particles on the surrounding flow increases. For large L, this randomness may far exceed the actual stochastic fluctuation. In this case, further spatial smoothing may be required to better represent the back-coupling effect. We have used a substantial number of droplets per cell; hence, no further spatial smoothing is carried out. Appropriate smoothing techniques will be considered in the future.

B. Interaction-Based Framework

Translating these physical models and their associated numerical procedures into a software package that is easy to modify and support is a nontrivial task. We attempt to meet these objectives through software modularity and commonality. Modularity is achieved by encapsulating the physical components in static libraries that are linked into the mixture modules to produce executables.

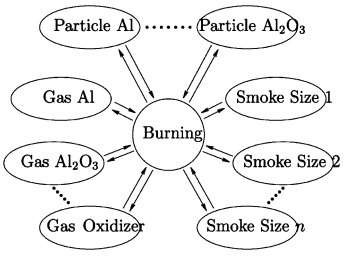

Fig. 1 Schematic representation of interactions for burning of aluminum particles.

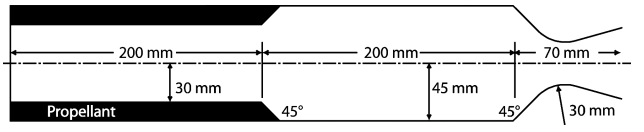

Fig. 2 Schematic of ONERA C1 geometry.

Commonality allows module developers to share code through user-defined data types, data structures, and procedures.

The implementation of the interactions among the physical components is encapsulated in a separate module. Instead of assigning an "owner" to each interaction, this module focuses on the interactions themselves. This is illustrated in Fig. 1 by taking the burning of aluminum particles as an example. Only so-called primary interactions (mass, momentum, or energy) need to be computed. The secondary (or implied) interactions (momentum or energy) are computed automatically.

The interpretation and implementation of such interactions have a number of advantages. First, they simplify the consistent and conservative transfer of mass, momentum, and energy between the physical components. Second, the burden on the developer of a physical module is reduced. Third, individual interactions may be deactivated in a consistent way to help in debugging or to study hypothetical scenarios. For example, it is very simple to study the effect of two-way coupling between aluminum particles and the gas mixture, or to investigate the impact of energy coupling between these two phases. By specifying several particle or smoke families, such studies may even be carried out concurrently.

In whole-system rocket simulations the fluid-dynamics code described is coupled with codes predicting the structural response of the propellant and its burn rate. Results of such whole-system computations were reported elsewhere by Fiedler et al.[34,35]

IV. Problem Setup

The ONERA C1 configuration (Fig. 2) described by Lupoglazoff and Vuillot,[36,37] Vuillot,[38] and Kourta[39] has been selected to perform computations with the present multiphase framework. The motor has a length of 0.47 m, a half-height of 0.045 m, and a width of 0.141 m. The grain length and height are 0.2 and 0.015 m, respectively; the grain tapers to zero thickness at an angle of 15 deg to create the second half of the main chamber. The location at which the propellant tapers is of importance since vortices are shed there. The original geometry definition considered by Lupoglazoff and Vuillot[36] included a symmetry plane. In the present computations, the symmetry plane was removed to allow for asymmetric disturbances. A converging–diverging nozzle is attached to the chamber motor. The computational grid consists of 317×60 nonuniformly distributed cells in the x and y directions, respectively. The grid resolution has been shown by various studies[37,39,40] to capture all the flow physics from shear layer development to acoustic coupling in the chamber.

The following boundary conditions have been imposed on the configuration (Fig. 2): A nonslip velocity is imposed for the head end, the nozzle walls, and the walls after the taper; supersonic outflow conditions are applied at the nozzle outlet; and fixed mass rate and temperature are set along the bottom and top injection surfaces. The propellant loading is set at 17.6% of aluminum by mass. The droplets are injected at zero velocity and are assumed to be in thermal equilibrium with the surrounding gas. Their initial composition consists of 80% aluminum and the remainder corresponds to a preexisting oxide cap. The viscosity is assumed to be constant. Tables 3 and 4 summarize the mixture and droplet properties used in these computations.

Table 3 Mixture properties

Quantity	Value	Unit
γ	1.14	——
C_p	2439.04	J/(kg · K)
T_{inj}	3387.0	K
$\dot{m}_{\text{tot}}$	21.201	kg/(m^2 · s)
μ	36.0×10^{-5}	kg/(m · s)

Table 4 Multiphase properties

Quantity	Value	Unit
ρ_{Al}	1766.0	kg/m^3
$T_{\text{Boil,Al}}$	3000.0	K
$C_{p,\text{Al}}$	1375.0	J/(kg · K)
$\rho_{Al_2O_3}$	1600.0	kg/m^3
T_{Boil,Al_2O_3}	4000.0	K
C_{p,Al_2O_3}	1100.0	J/(kg · K)
$T_{p,\text{inj}}$	3387.0	K
$\dot{m}_p$	3.1622	kg/(m^2 · s)
ϕ_p	0.176	

Table 5 Test matrix for computations

Run	d_s, μm	Distribution
1	1.5	SLD-A
2	1.5	SLD-B
3	1.5	LND
4	5.0	SLD-A
5	5.0	SLD-B
6	5.0	LND

The values for the densities of the aluminum and alumina correspond to mean values obtained from the following relationships[8,41]:

$$\rho_{\text{Al}} = 2385 - 0.28(T - 933), \qquad \rho_{Al_2O_3} = 5632 - 1.127T \quad (39)$$

The goals of the present study are to investigate the effects of droplet size distributions at injection and smoke particle sizes on the flow dynamics in the chamber. Table 5 summarizes the test matrix for the various runs. The droplet distributions used have been described in Sec. II.G. For the skewed logarithmic distribution, two profiles have been chosen: the first type (SLD-A) has minimum, peak, and maximum diameters of 5, 30, and 240 μm, respectively, with a standard deviation of 1.3, whereas the second type (SLD-B) has the corresponding values of 5, 30, and 190 μm, respectively, with a standard deviation of 1.0. These values have been chosen from the new agglomeration model for a representative propellant.[22] The logarithmic normal distribution (LND) has a peak diameter and standard deviation of 30 μm and 0.25, respectively. A superdroplet loading factor has been chosen such that a total of approximately 110,000 droplets are instantaneously tracked in the computational domain. This results in superdroplet loading factors of 10, 18, and 95 for the distributions SLD-A, SLD-B, and LND, respectively. Figures 3a–3c present the three distributions investigated at the injecting surfaces. Smoke particles are assumed to be generated at a fixed diameter with values of 1.5–5 μm. The simulations are run on a 60-processor IBM SP3 computer system and a typical computation for a representative time span of 4 ms requires approximately 12 CPU hours.

V. Results

A. Instantaneous Fields

Uncoupled single-phase simulations were initially performed and the results showed that the flow forms an instability at the corner,

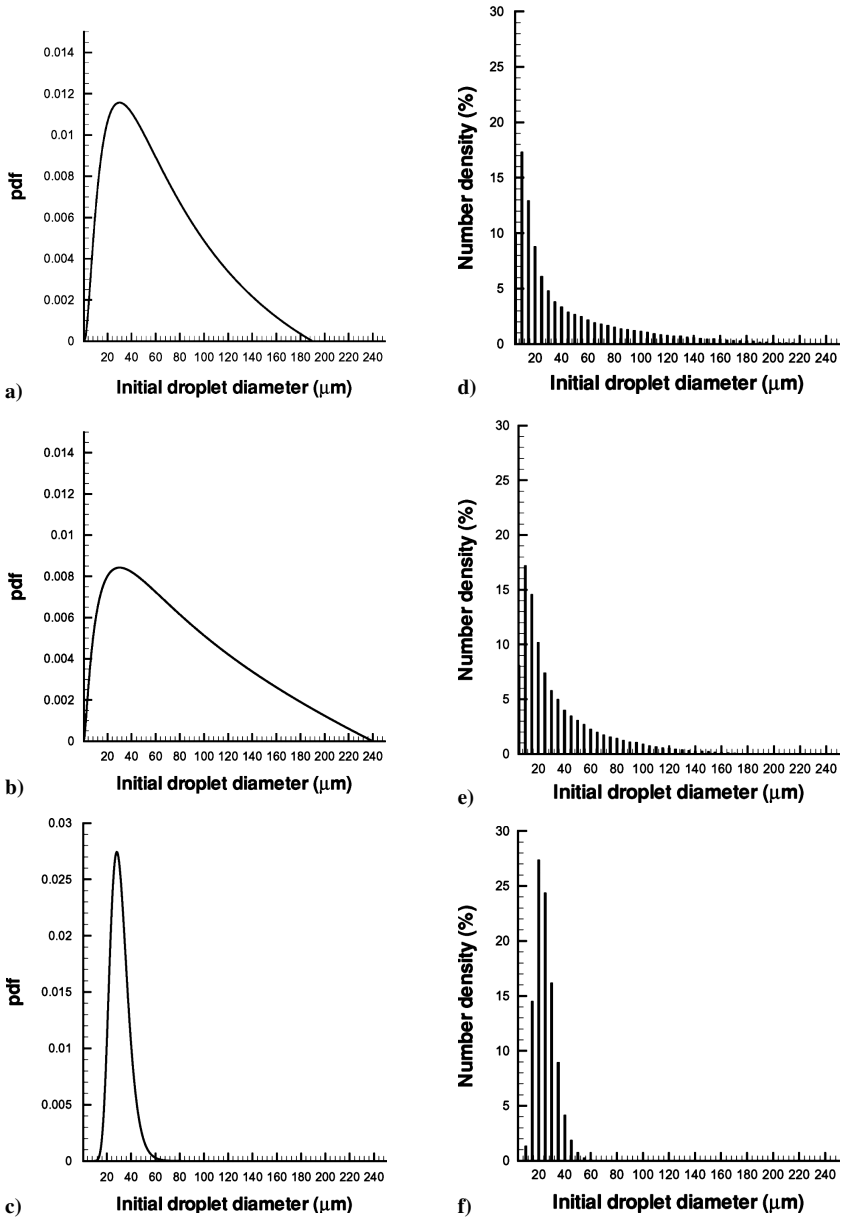

Fig. 3 Histograms of the pdf and number density percentage with droplet diameter a–c) at the injection surface and d–f) at the nozzle inlet ($x = 0.4$ m): a and d) run 1, b and e) run 2, and c and f) run 3.

leading to Kármán-like vortex shedding in the noninjection section of the chamber. A primary shedding frequency of 2568 Hz was obtained, comparing well with the secondary longitudinal mode of the chamber, which exhibits a frequency of 2570 Hz (Refs. 17, 36, and 39). Further details of the single-phase flow dynamics have been discussed by Najjar et al.[42]

Figures 4–6 show the mixture spanwise-vorticity field, the mixture temperature, the droplet location (colored by the diameter), and the smoke concentration for runs 1, 2, and 3. It is observed that the flow maintains its unsteady nature for runs 1 and 2 with several large-scale vortices existing in the main chamber, whereas, for run 3, the flow reverts to a laminarized state similar to the nonreactive coupled case.[42] Further, the temperature field maintains a high value along the centerline for runs 1 and 2, whereas it is substantially higher throughout the chamber for run 3. The droplet distributions in the chamber are strongly affected by the flow dynamics. By comparing Figs. 4c, 5c, and 6c, the droplets are seen to avoid regions of high vorticity. The edges of the laminarized shear layers are clearly captured in Fig. 6c. Further, it is observed that the droplet distributions obtained for runs 1 and 2 are quite similar, demonstrating that the results are insensitive to the details of SLD. However, when the droplet distributions for these two runs are compared with the LND configuration (run 3), substantial differences are observed. Because the LND configuration is extensively used in industry, its validity as a distribution to describe all types of propellants could be questioned in view of the present results. Finally, the distributions of the smoke concentration, presented in Figs. 4d, 5d, and 6d, are low near the injection walls, increasing rapidly toward the core, as expected. However, the smoke concentrations are higher for run 3 compared to runs 1 and 2.

For the remaining cases, runs 4–6, in which the smoke diameter size was increased to 5 μm, no significant changes in the overall multiphase flow dynamics have been captured for the mixture, the droplet locations, on the corresponding smoke concentrations with respect to runs 1–3. Hence, it can be concluded that the current simulations are quite insensitive to the smoke diameter size. Further, a simulation with a smoke diameter size of 0.5 μm for SLD-A has been performed and the results were similar to run 1. In the remainder of this article, we will focus our attention on the results obtained in runs 1–3.

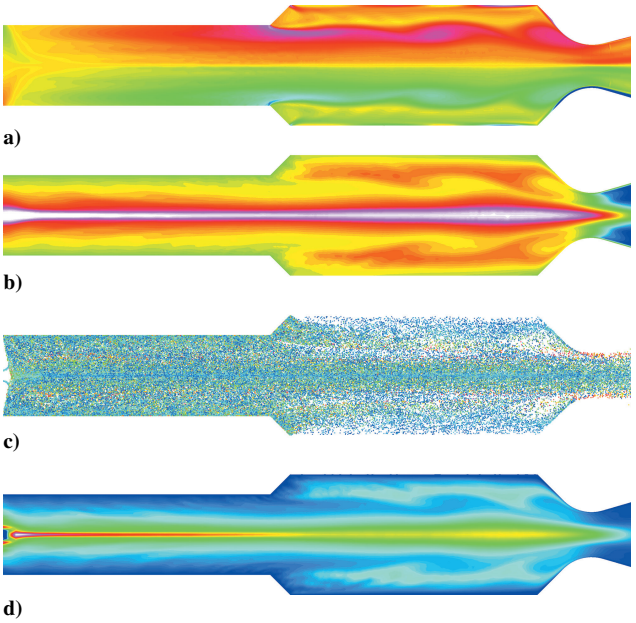

Fig. 4 Results for ONERA C1 configuration with run 1 at $t = 10$ ms: a) spanwise vorticity [$(\omega_{z,\min}, \omega_{z,\max}, \Delta\omega_z) = (-5 \times 10^4\ \text{s}^{-1}, 5 \times 10^4\ \text{s}^{-1}, 10^3\ \text{s}^{-1})$]; b) temperature [$(T_{\min}, T_{\max}, \Delta T_z) = (3000, 4000, 20\ \text{K})$]; c) droplet positions colored by diameter [$(d_{p,\min}, d_{p,\max}, \Delta d_p) = (10, 250, 10\ \mu\text{m}$] with 2.5 and 5 μm); and d) smoke concentration [$(C_{s,\min}, C_{s,\max}, \Delta C_s) = (5 \times 10^{-4}, 6 \times 10^{-2}, 5 \times 10^{-4}\ \text{kg/m}^3)$].

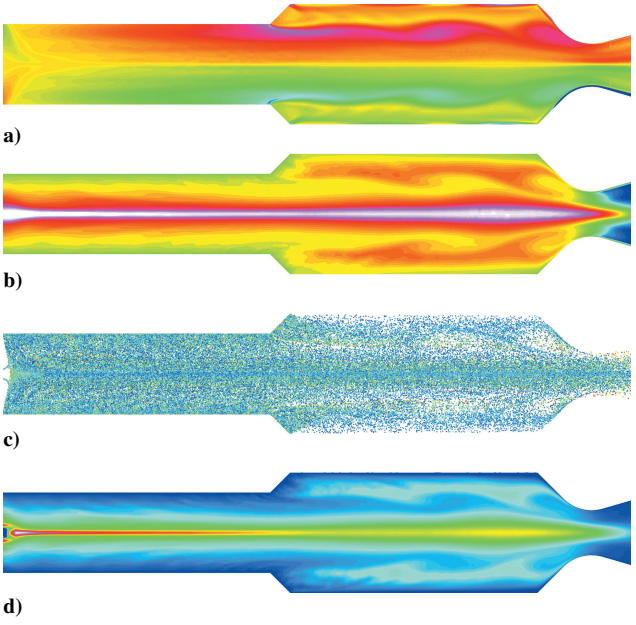

Fig. 5 Results for ONERA C1 configuration with run 2 at $t = 10$ ms: a) spanwise vorticity, b) temperature, c) droplet positions colored by diameter, and d) smoke concentration. Contour levels are the same as in Fig. 4.

B. Statistics

Once the flow reaches a quasi-steady state, statistics are gathered for over 4 ms, representing approximately 10 shedding cycles in the uncoupled single phase simulations. Individual data sets of the 80 instantaneous multiphase flowfields have been saved, corresponding to a time interval separation of 0.05 ms. A streamwise location at the nozzle entrance ($x = 0.40$ m) is selected to assess the effects of injected droplet diameter distribution on the multiphase flow statistics. Two separate sets of conditional statistics have been determined. In the first set, the data were binned according to droplet diameters. In the second set, the data were binned according to their y coordinates.

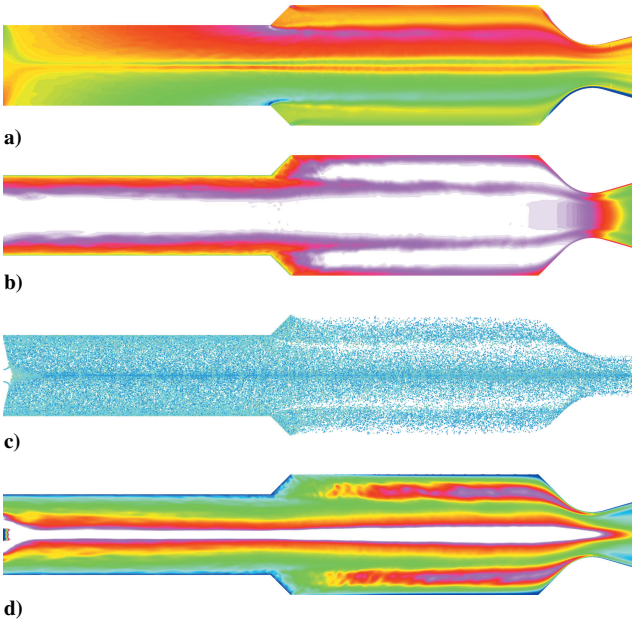

Fig. 6 Results for ONERA C1 configuration with run 3 at $t = 10$ ms: a) spanwise vorticity, b) temperature, c) droplet positions colored by diameter, and d) smoke concentration. Contour levels are same as those in Fig. 4.

Figures 3d, 3e, and 3f show histograms of the normalized number density varying with the droplet diameter for runs 1, 2, and 3, respectively. It is observed that the distribution is broad for runs 1 and 2, whereas it is quite narrow for run 3. For the current motor configuration, the droplets are seen to retain characteristics of their initial distributions. The corresponding histograms of the droplet aluminum composition, ϕ_{Al}, are plotted in Fig. 7. The smaller droplet sizes have completely exhausted their aluminum contents, whereas the larger droplets retain most of their initial content (72–78%). A plateau is rapidly reached for droplet diameters above 50 μm. Section V.C will provide further insight into these effects. The alumina composition can easily be inferred from the mass conservation as $\phi_{\text{Al}_2\text{O}_3} = 1 - \phi_{\text{Al}}$. Hence, for small droplets, the alumina composition is 100%, but it decreases rapidly to 22–28% for the larger droplets. Most rocket motors are designed so that the aluminum droplets burn out before entering the nozzle. The present rocket-like geometry is just a computational model, originally chosen to test the flow.[36,39] The residence time of the larger droplets is not sufficiently long to achieve complete burnout. Clearly droplets of larger than about 10 μm at injection are not appropriate for the present configuration if complete burnout is desired.

Figure 8 shows the y distribution of the time-averaged number density, droplet aluminum composition, and mass-mean diameter. It is observed that the number density is symmetrically distributed about the centerline with smaller peaks close to the bottom and top walls. The results obtained for run 3 present a strong peak at the centerline whereas those for runs 1 and 2 are similar. In Fig. 8b, the distributions of the droplet aluminum composition are symmetric with respect to the centerline, reaching a plateau in the chamber core while dropping rapidly near the walls. The composition is observed to be higher for runs 1 and 2 by 20% over run 3, and this is due to the predominantly smaller size of the droplets in run 3. The mass-mean diameter d_{43} defined as

$$d_{43} = \frac{\sum d_p^4}{\sum d_p^3} \tag{40}$$

is plotted in Fig. 8c for the three runs. It is seen that run 3 has the flattest distribution, with a mean value of approximately 30 μm, whereas the mass-mean diameters computed for runs 1 and 2 are significantly higher, reaching peak values of 160 μm. The distributions are seen to drop dramatically to a value close to that of run

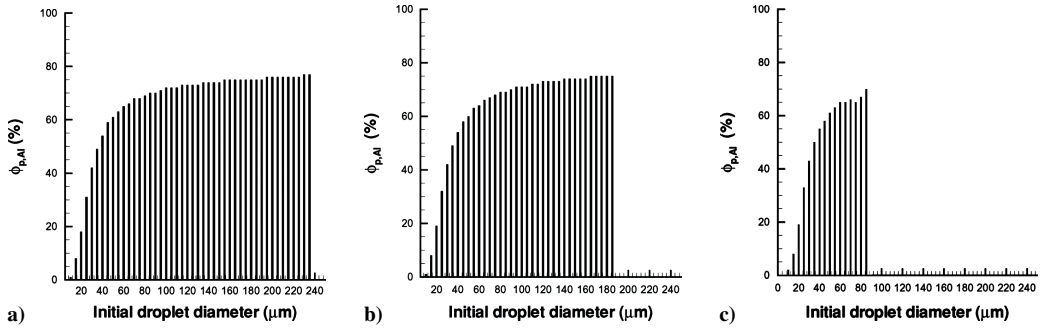

Fig. 7 Histograms of the aluminum composition, $\phi_{p,\mathrm{Al}}$, with droplet diameter at the nozzle inlet ($x = 0.4$ m): a) run 1, b) run 2, and c) run 3.

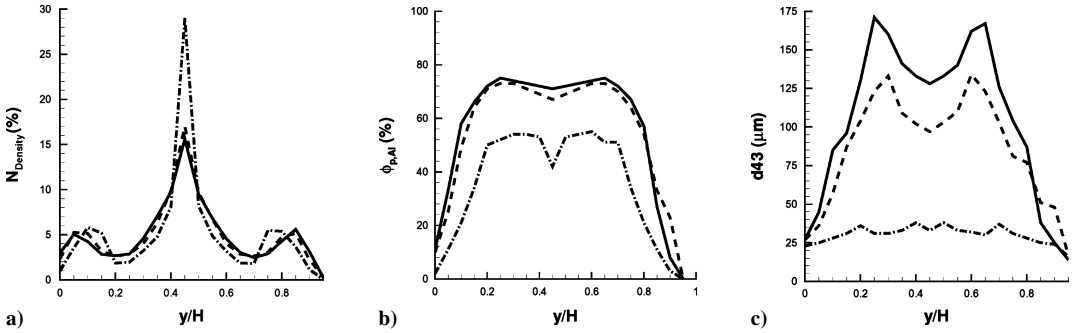

Fig. 8 Transverse distribution at the nozzle inlet ($x = 0.4$ m): a) number density percentage, b) aluminum composition, and c) mass-mean diameter; ——, run 1; - - - -, run 2; and –·–, run 3.

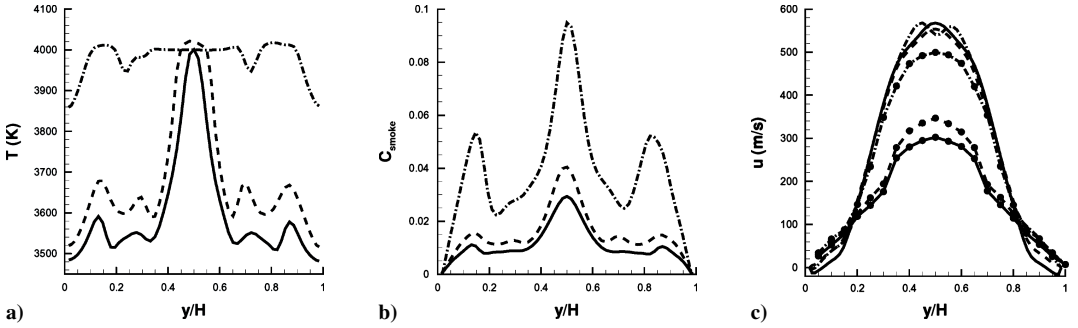

Fig. 9 Transverse distribution at the nozzle inlet $x = 0.40$ m: a) mixture temperature, b) alumina smoke concentration, and c) mixture and droplet streamwise velocity; ——, run 1; - - - -, run 2; and –·–, run 3; no symbols for mixture; circles for Lagrangian droplets.

3 near the rocket motor walls. Further, a valley is obtained at the centerline.

Figure 9 shows the y distribution of time-mean mixture temperature, smoke concentration, and mass-mean diameter. The mixture temperature distribution is highest for run 3 with a value very close to the aluminum oxide boiling point of 4000 K. This clearly shows how the full heat-release capability, described in Sec. II.C, sets a plateau value for the mixture temperature where clipping occurs when the threshold value is exceeded. The distributions obtained for runs 1 and 2 are significantly lower in the main chamber, except that a peak value is reached near the centerline, where the droplets are seen to agglomerate (see Fig. 5b). In Fig. 9b, the smoke concentration is seen to have a peak at the centerline and in the core region of the shear layers. As observed in Fig. 6c, the results from run 3 show higher levels of smoke concentration. Finally, the streamwise component of the mixture and droplet streamwise velocities are plotted in Fig. 9c. The three runs have similar time-averaged values; however, run 3 shows that time-averaged velocity of the droplet is more in equilibrium with the mixture, whereas the droplets in runs 1 and 2 lag the fluid. The time-averaged results provide further insight into the differences observed in Figs. 4–6. Because the Lagrangian field for run 3 has the highest equilibrium and thus the timescales between the droplets and the mixture are comparable, the droplets will substantially modify the mixture field.

C. Verification for Residence Time and Burning Droplet Diameter

The current coupled multiphase simulations are challenging to validate. Rocket chambers are very hostile environments for experimental instrumentations due to the high temperature. For this reason, detailed experimental data for validating multiphase flow simulations such as those presented here do not appear to exist. The only possibility of checking the results is thus to compare them with theoretical models. To this end, we compare the droplet residence time in the rocket chamber, t_{res}, and the diameter of the convecting burning droplet with simple theoretical predictions. The streamwise location evolution of the droplet, derived from the streamwise velocity [see Eq. (8)] is given by

$$\tau_p \frac{\mathrm{d}^2 x_p}{\mathrm{d}t^2} + \frac{\mathrm{d}x_p}{\mathrm{d}t} - u_m(x_p) = 0 \tag{41}$$

This equation is subject to the initial streamwise location and velocity of the droplet, $x_{p,0}$ and $u_{p,0}$, respectively. The mixture streamwise velocity, u_m, is typically a function of both the streamwise and transverse locations of the droplet. Here we simplify the theoretical analysis by considering the mixture velocity to be that along the motor centerline. The rationale for this assumption is that the droplets quickly approach the centerline. To a good degree, the mixture

velocity can be approximated as

$$u_m = \begin{cases} x_p/L_1 U_{\max} & \text{for} \quad 0 \le x_p \le L_1 \\ U_{\max} & \text{for} \quad L_1 \le x_p \le L_2 \end{cases} \tag{42}$$

where L_1 is the length of the first segment that has the propellant, L_2 is the length of the entire motor, and $U_{\max}$ was found to have a value of 500 m/s.

The closed form solution of Eq. (41) in the upstream segment of the rocket ($0 \le x_p \le L_1$) is

$$x_p(t) = A_p \exp^{(\alpha_1 t)} + B_p \exp^{(\alpha_2 t)}$$

$$u_p(t) = A_p \alpha_1 \exp^{(\alpha_1 t)} + B_p \alpha_2 \exp^{(\alpha_2 t)}, \qquad \alpha_{1,2} = (-1 \pm \beta)/2\tau_p$$

$$\beta = \sqrt{1 + 4\tau_p U_{\max}/L_1}$$

$$A_p = \tfrac{1}{2}[x_{p,0} + (2\tau_p/\beta)(u_{p,0} + x_{p,0}/2\tau_p)]$$

$$B_p = \tfrac{1}{2}[x_{p,0} - (2\tau_p/\beta)(u_{p,0} + x_{p,0}/2\tau_p)] \tag{43}$$

The closed-form solution of Eq. (41) in the aft segment of the motor chamber is given by

$$x_{p,2}(t) = U_{\max} t + \tau_p [U_{\max} - u_{p,1}(t)](\exp^{-t/\tau_p} - 1) + L_1$$

$$u_{p,2}(t) = U_{\max} + [U_{\max} - u_{p,1}(t)] \exp^{-t/\tau_p} \tag{44}$$

where $u_{p,1}(t)$ is the droplet streamwise velocity at L_1 obtained from Eq. (43).

The droplet residence time in each section is determined by inverting Eqs. (43) and (44). We follow the evolution of a set of droplets with varying diameters (10, 50, 100, and 200 μm) injected at two separate initial locations: near the head end ($x = 0.02$ m) and midsection ($x = 0.1$ m). Figure 10 shows the variation of the residence time for initial droplet diameters in different ranges. The residence time varies from 1 to 9 ms and the agreement with the analytical solutions is quite satisfactory in Fig. 10a. For the particles injected past the streamwise location $x = 0.1$ m, some differences can be observed, and this perhaps is due to neglecting the flow turning effects in the droplet evolution [Eq. (41)]. Figure 10c plots the residence time for a particle injected at the head-end till it reaches the nozzle inlet. Again the comparison with the analytical solution is good.

Figure 11 compares the droplet streamwise velocity obtained in the simulation with those determined from the analytical solutions at two streamwise locations of 0.2 and 0.4 m. It is seen that the computed droplet velocities are larger than the analytic predictions and the difference increases further downstream.

Finally, since the droplet diameter changes temporally due to the burning process, its evolution is analytically formulated. Starting with the droplet mass burning evolution [see Eq. (16)], and reformulating in terms of droplet diameter, the evolution of the droplet diameter is formulated in terms of an ordinary differential equation as follows:

$$\frac{\pi \rho_p d_p^2}{2} \frac{\mathrm{d}d_p}{\mathrm{d}t} = -\kappa_p d_p^{1.1} \tag{45}$$

where κ_p is a variable representing all of the terms in the Widener–Beckstead model except the diameter,

$$\kappa_p = c\rho_{\mathrm{Al}} T^{1.57}(\boldsymbol{x}_p) p^{0.2}(\boldsymbol{x}_p) \chi_{\mathrm{eff}}^{0.39} \mathcal{D}_{\mathrm{rel}} \psi_{\mathrm{Al}} \tag{46}$$

Hence, the closed form of the burning droplet diameter, as it evolves in time, is

$$d_p^{1.9}(t) = d_{p,0}^{1.9} - (3.8/\pi\rho_p)\kappa_p t \tag{47}$$

It is to be noted that this formula does not account for alumina deposition; however, its contribution is expected to be minimal. Figure 12 shows the variation of the droplet diameter with the initial

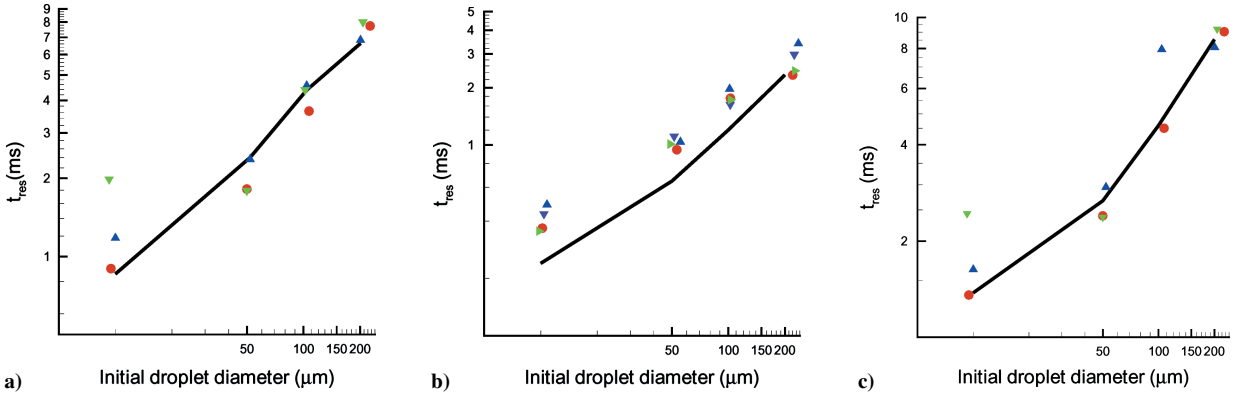

Fig. 10 Variation of residence time with initial droplet diameter for particles injected from a) $x = 0.02$ m and moving to $x = 0.2$ m, b) $x = 0.1$ m and moving to $x = 0.2$ m, and c) $x = 0.02$ m and moving to $x = 0.4$ m. Symbols (lines) represent values obtained from multiphase flow code (analytical solution).

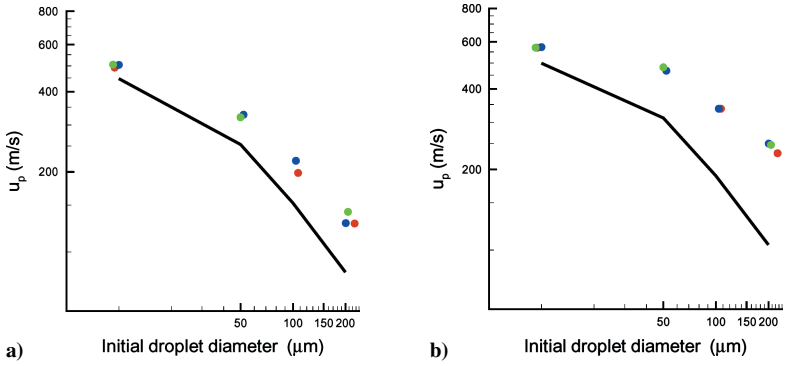

Fig. 11 Variation of droplet streamwise velocity with initial droplet diameter for particles injected from a) $x = 0.02$ m and moving to $x = 0.2$ m and b) $x = 0.02$ m and moving to $x = 0.4$ m. Symbols (lines) represent values obtained from multiphase flow code (analytical solution).

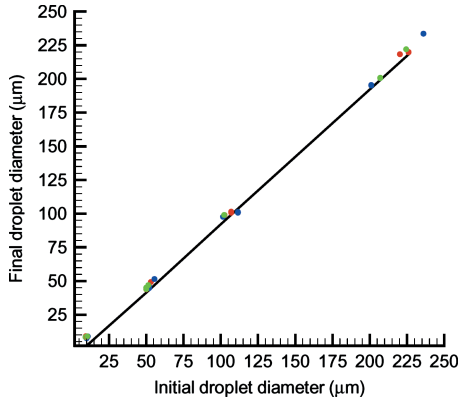

Fig. 12 Variation of droplet diameter with initial droplet diameter for particles injected at $x = 0.02$ m symbols (lines) represent values obtained from multiphase flow code (analytical solution).

injection diameter. The droplets have been injected near the head end and their diameters are obtained at the nozzle inlet. Comparison with Eq. (47) shows quite satisfactory agreement. It is interesting to note that the droplets with the larger diameters do not burn as completely as the smaller ones. As addressed earlier, this incomplete burning is an artifact of the chosen geometry in which the residence time for the droplets larger than 10 μm is not enough for complete burnout.

VI. Summary

The modeling and simulation of the flow in solid-propellant rockets from first principles is extremely challenging. Among the modeling difficulties to be addressed are complex evolving geometries, turbulence, and multiphase flow with chemically reacting disperse phase. Apart from the need for robust and efficient numerical techniques, one of the main computational challenges is posed by strong interactions among various phenomena. We have developed a framework to handle these complex multiphysics processes and included advanced computational capabilities including full heat release for the burning process, a new formalism for the smoke, a conversing two-coupling scheme, and a stochastic-based droplet injection model.

Multiphase flow simulations in a typical configuration have been performed with burning aluminum droplets generating aluminum oxide smoke. Droplet size distributions have been investigated and two models have been used: one based on a specific propellant distribution, the other on subscale propellant packing and combustion models mimicking real propellant behavior. The effects of the distributions on the chamber flow dynamics and specifically at the nozzle inlet are observed to be quite range. The smoke particle size is seen to affect the overall chamber dynamics minimally. Verifications of the residence time and burning droplet diameter compare quite well with simple analytical predictions. In the present configuration, small-sized droplets quickly consume their aluminum, whereas larger droplets move in the chamber with lower combustion efficiency. Future studies are being undertaken to gain further insight into multiphase flow dynamics for full-scale rockets, such as the RSRM booster with inhibitors and submerged nozzle.

Acknowledgments

The Center for Simulation of Advanced Rockets is supported by the Department of Energy through the University of California under Subcontract B341494. We thank T. Jackson and W. Dick.

References

[1]Price, E. W., and Sigman, R. K., "Combustion of Aluminized Solid Propellants," *Solid Propellant Chemistry, Combustion and Motor Interior Ballistics,* edited by V. Yang, T. Brill, and W. Ren, Vol. 185, Progress in Astronautics and Aeronautics, AIAA, New York, 2000, pp. 663–668.

[2]Taylor, G. I., "Fluid Flow in Regions Bounded by Porous Surfaces," *Proceedings of the Royal Society of London, Series A*, Vol. 234, 1956, pp. 456–475.

[3]Proudman, I., "An Example of Steady Laminar Flow at Large Reynolds Number," *Journal of Fluid Mechanics*, Vol. 9, 1962, pp. 593–602.

[4]Culick, F. E. C., "Rotational Axisymmetric Mean Flow and Damping of Acoustic Waves in Solid Propellant Rocket Motors," *AIAA Journal*, Vol. 4, No. 8, 1966, pp. 1462–1464.

[5]Coats, D., Dunn, S., and French, J., "Improvements to the Solid Performance Program (SPP)," AIAA Paper 2003-4504, July 2003.

[6]Majdalani, J., Vyas, A. B., and Flandro, G. A., "Higher Mean-Flow Approximation for a Solid Rocket Motor with Radially Regressing Walls," *AIAA Journal*, Vol. 40, No. 9, 2002, pp. 1780–1788.

[7]Majdalani, J., "Physicality of Core Flow Models in Rocket Motors," *Journal of Propulsion and Power*, Vol. 19, No. 1, 2003, pp. 156–159.

[8]Cesco, N., Lavergne, G., and Estivalezes, J. L., "Simulation of the Two Phase Flow in Solid Rocket Motors," AIAA Paper 96-2640, July 1996.

[9]Godfroy, F., and Guery, J. F., "Unsteady Eulerian Two-Phase Flow Analysis of Solid Rocket Motor Slag," AIAA Paper 97-2859, July 1997.

[10]Laubacher, B. A., "Internal Flow Analysis of Large L/D Solid Rocket Motors," AIAA Paper 2000-3803, July 2000.

[11]Eaton, A. M., Ewing, M. E., and Bailey, K. M., "Modeling the Gas Dynamics Environment in a Subscale Solid Rocket Test Motor," AIAA Paper 2001-3584, July 2001.

[12]Dupays, J., Wey, S., and Fabignon, Y., "Steady and Unsteady Reactive Two-Phase Computations in Solid Rocket Motors with Eulerian and Lagrangian Approaches," AIAA Paper 2001-3871, July 2001.

[13]Daniel, E., "Eulerian Approach for Unsteady Two-Phase Solid Rocket Flows with Aluminum Particles," *Journal of Propulsion and Power*, Vol. 16, No. 2, 2000, pp. 309–317.

[14]Sabnis, J. S., and deJong, F. J., "Calculation of the Two-Phase Flow in an Evaporating Spray Using an Eulerian–Lagrangian Analysis," AIAA Paper 90-0447, Jan. 1990.

[15]Madabhushi, R. K., Sabnis, J. S., deJong, F. J., and Gibeling, H. J., "Calculation of Two-Phase Aft-Dome Flowfield in Solid Rocket Motors," *Journal of Propulsion and Power*, Vol. 7, No. 2, 1991, pp. 178–184.

[16]Sabnis, J. S., deJong, F. J., and Gibeling, H. J., "A Two-Phase Restricted Equilibrium Model for Combustion of Metalized Solid Propellant," AIAA Paper 92-3509, July 1992.

[17]Morfouace, V., and Tissier, P. Y., "Two-Phase Flow Analysis of Instabilities Driven by Vortex-Shedding in Solid Rocket Motors," AIAA Paper 95-2733, July 1995.

[18]Ciucci, A., Iaccarino, G., Amato, M., "Numerical Investigation of 3D Two-Phase Turbulent Flows in Solid Rocket Motors," AIAA Paper 98-3966, July 1998.

[19]Lupoglazoff, N., Vuillot, F., Dupays, J., and Fabignon, Y., "Numerical Simulations of the Unsteady Flow Inside Segmented Solid-Propellant Motors with Burning Aluminum Particles," AIAA Paper 2002-0784, Jan. 2002.

[20]Salita, M., "Quench Bomb Investigation of Al_2O_3 Formation from Solid Rocket Propellants. II. Analysis of Data," *25th JANNAF Combustion Meeting*, CPIA 498, Vol. 1, 1988, pp. 185–197.

[21]Whitesides, R. H., Dill, R. A., and Purinton, D. C., "Application of Two-Phase CFD Analysis to the Evaluation of Asbestos-Free Insulation in the RSRM," AIAA Paper 97-2861, July 1997.

[22]Jackson, T. L., Najjar, F. M., and Buckmaster, J., "New Aluminum Agglomeration Models and Their Use in Solid-Propellant-Rocket Simulations," *Journal of Propulsion and Power*, Vol. 21, No. 5, 2005, pp. 925–936.

[23]Ferry, J., and Balachandar, S., "Equilibrium Expansion for the Eulerian Velocity of Small Particles," *Powder Technology*, Vol. 125, Nos. 2–3, 2002, pp. 131–139.

[24]Bagchi, P., and Balachandar, S., "Steady Planar Straining Flow past a Rigid Sphere at Moderate Reynolds Number," *Journal of Fluid Mechanics*, Vol. 466, 2002, pp. 365–407.

[25]Widener, J. F., and Beckstead, M. W., "Aluminum Combustion Modeling in Solid Propellant Combustion Products," AIAA Paper 98-3824, July 1998.

[26]Shaw, R., "Particle-Turbulence Interactions in Atmospheric Clouds," *Annual Review of Fluid Mechanics*, Vol. 35, 2003, pp. 183–227.

[27]Ferry, J., and Balachandar, S., "A Fast Eulerian Method for Disperse Two-Phase Flow," *International Journal of Multiphase Flow*, Vol. 27, No. 7, 2001, pp. 1199–1226.

[28]Najjar, F. M., Haselbacher, A., Ferry, J. P., Wasistho, B., Balachandar, S., and Moser, R. D., "Large-Scale Multiphase Large-Eddy Simulation of Flows in Solid-Rocket Motors," AIAA Paper 2003-3700, June 2003.

[29]Brady, J. F., "From Proteins to Peas: Diffusion Across Scales," IUTAM Symposium on Computational Approached to Disperse Multiphase Flows, Argonne National Lab., Argonne, IL, Oct. 2004; also Proceedings, Kluwer Academic (to be published).

[30]Najjar, F. M., Haselbacher, A., Ferry, J. P., and Balachandar, S., "Rocpart Developer's Guide," Center for Simulation of Advanced Rockets, Univ. of Illinois, Urbana, IL, Jan. 2005.

[31]Jameson, A., Schmidt, W., and Turkel, E., "Numerical Solutions of the Euler Equations by Finite-Volume Methods Using Runge–Kutta Time-Stepping Schemes," AIAA Paper 81-1259, Jan. 1981.

[32]Gropp, W., Lusk, E., and Skelljum, A., *Using MPI: Portable Parallel Programming with the Message-Passing Interface*, MIT Press, Cambridge, MA, 1994.

[33]Blazek, J., "Flow Simulation in Solid Rocket Motors Using Advanced CFD," AIAA Paper 2003-5111, July 2003.

[34]Fiedler, R., Jiao, X., Namazifard, A., Haselbacher, A., Najjar, F., and Parsons, I. D., "Coupled Fluid-Structure 3-D Solid Rocket Motor Simulations," AIAA Paper 2001-3954, July 2001.

[35]Fiedler, R., Breitenfeld, M. S., Jiao, X., Haselbacher, A., Geubelle, P., Guoy, D., and Brandyberry, M., "Simulations of Slumping Propellant and Flexing Inhibitors in Solid Rocket Motors," AIAA Paper 2002-4341, July 2002.

[36]Lupoglazoff, N., and Vuillot, F., "Numerical Simulation of Vortex Shedding Phenomenon in 2D Test Case Solid Rocket Motors," AIAA Paper 92-0776, July 1992.

[37]Lupoglazoff, N., and Vuillot, F., "Parietal Vortex Shedding as a Cause of Instability for Long Solid Propellant Motors–Numerical Simulations and Comparisons with Firing Tests," AIAA Paper 96-0761, Jan. 1996.

[38]Vuillot, F., "Vortex Shedding Phenomena in Solid Rocket Motors," *Journal of Propulsion and Power*, Vol. 11, No. 4, 1995, pp. 626–639.

[39]Kourta, A., "Computation of Vortex Shedding in Solid Rocket Motors Using Time-Dependent Turbulence Model," *Journal of Propulsion and Power*, Vol. 15, No. 3, 1999, pp. 390–400.

[40]Tissier, P. Y., Godfroy, F., and Jacquemin, P., "Simulation of Three Dimensional Flows inside Solid Propellant Rocket Motors Using a Second Order Finite Volume Method Application to the Study of Unstable Phenomena," AIAA Paper 92-3275, July 1992.

[41]Iida, T., and Guthrie, P. I. L., *The Physical Properties of Liquid Metals*, Clarendon, Oxford, 1988.

[42]Najjar, F. M., Ferry, J., Wasistho, B., and Balachandar, S., "Full-Physics Large-Scale Multiphase Large Eddy Simulations of Flow Inside Solid Rocket Motors," AIAA Paper 2002-4343, July 2002.

T. Lin
Associate Editor

Color reproductions courtesy of the Center for Simulations of Advanced Rockets.